Magnetically programmable surface acoustic wave filters: device concept and predictive modeling

Michael K. Steinbauer, Peter Flauger, Matthias Küß, Stephan Glamsch, Emeline D. S. Nysten, Matthias Weiß, Dieter Suess, Hubert J. Krenner, Manfred Albrecht, Claas Abert

Angaben zur Veröffentlichung / Publication details:

Steinbauer, Michael K., Peter Flauger, Matthias Küß, Stephan Glamsch, Emeline D. S. Nysten, Matthias Weiß, Dieter Suess, Hubert J. Krenner, Manfred Albrecht, and Claas Abert. 2026. "Magnetically programmable surface acoustic wave filters: device concept and predictive modeling." *npj Spintronics* 4 (1): 13. https://doi.org/10.1038/s44306-026-00132-4.

npj | spintronics

https://doi.org/10.1038/s44306-026-00132-4

Magnetically programmable surface acoustic wave filters: device concept and predictive modeling

Check for updates

Michael K. Steinbauer[1,2,3] ✉, **Peter Flauger**[1,2], **Matthias Küß**[4], **Stephan Glamsch**[4], **Emeline D. S. Nysten**[5], **Matthias Weiß**[5], **Dieter Suess**[1,2], **Hubert J. Krenner**[5], **Manfred Albrecht**[4] & **Claas Abert**[1,2]

Filtering surface acoustic wave (SAW) signals of specified frequencies depending on the strength of an external magnetic field in a magnetostrictive material has garnered significant interest due to its potential scientific and industrial applications. Here, we propose a device that achieves selective SAW attenuation by instead programming its internal magnetic state. To this end, we perform micromagnetic simulations for the magnetoelastic interaction of the Rayleigh SAW mode with spin waves (SWs) in exchange-decoupled Co/Ni islets on a piezoelectric $LiTaO_3$ substrate. Due to the islets exhibiting perpendicular magnetic anisotropy, the stray-field interaction between them leads to a shift in the SW dispersion depending on the magnetic alignment of neighboring islets. This significantly changes the efficiency of the magnetoelastic interaction at specified frequencies. We predict changes in SAW transmission of 52.0 dB/mm at 3.8 GHz depending on the state of the device. For the efficient simulation of the device, we extend a prior energy conservation argument based on analytical solutions of the SW to finite-difference numerical calculations, enabling the modeling of arbitrary magnetization patterns like the proposed islet-based design.

Surface acoustic wave (SAW) devices are integral to the modern telecommunications infrastructure, where they have already functioned as high-performance band-pass filters for decades[1–3]. The foundational principle for their application as filters was established with the introduction of specially shaped electrodes, called interdigital transducers (IDTs), on piezoelectric substrates[4].

An alternating voltage applied to a transmitting IDT excites SAWs within the substrate. These waves propagate across the substrate to a receiving IDT, where they are converted back to an electrical signal. The geometric configuration of the IDT dictates the resonance frequency at which SAWs can be excited, along with higher-order harmonics. This inherent frequency selectivity enables the precise bandpass filtering characteristic of SAW devices, while their small size and operating range in the radio frequency (RF) regime make them ideal for use in hand-held devices like smartphones[5–7].

While a different kind of filter, the bulk acoustic wave (BAW) filter, is currently dominant for high-frequency applications in the telecommunications industry[8,9], SAW devices remain relevant. This is because the basic functionality of SAW devices can be extended by modifying the substrate between the IDTs in various ways. This modification enables their application as lab-on-a-chip platforms for advancements across diverse disciplines, including physics, chemistry, and medicine[10–13]. A significant area of interest involves the interaction of these devices with magnetism. Magneto-elastic coupling is historically well-established for its ability to alter the properties of a SAW[14,15]. Recently, significant focus has been put on these interactions in the RF regime[16,17]. Specifically, the excitation of spin waves (SWs) via the magnetoelastic effect has emerged as a promising tool in magnonics, offering numerous potential applications[18,19]. One such application is the ability to absorb specific frequencies, dependent on the strength of an applied external magnetic field, when the SAW interacts with a magnetic thin film[20–24].

This can be achieved because SAW attenuation is only significant at frequencies where its dispersion relation intersects with that of the SW. There, the SAW's energy is transduced to a SW, where it then dissipates via Gilbert damping[25–27]. The crossover point of the dispersion relations can be precisely tuned by adjusting the strength of an external magnetic field, as the field shifts the SW dispersion relation, thereby repositioning the resonance point to a desired frequency. By tuning this point to the band-pass frequency, signals are attenuated, whereas when detuned, the signal passes without attenuation, resulting in highly efficient signal filtering. However,

---

[1]University of Vienna, Faculty of Physics, Physics of Functional Materials, Vienna, Austria. [2]University of Vienna, Research Platform MMM Mathematics-Magnetism-Materials, Vienna, Austria. [3]University of Vienna, Vienna Doctoral School in Physics, Vienna, Austria. [4]University of Augsburg, Institute of Physics, Augsburg, Germany. [5]Universität Münster, Physikalisches Institut, Münster, Germany. ✉e-mail: michael.karl.steinbauer@univie.ac.at

implementing such a device would necessitate the continuous operation of a variable electromagnet, which is undesirable for many potential applications.

In this study, we propose a different method to deliberately shift the SW dispersion, where we utilize exchange-decoupled, but stray-field interacting, thin magnetic islets with out-of-plane (OOP) magnetization and a large magnetic moment (see Fig. 1). The magnetization direction of each islet, influenced by the device's magnetic history, can align along either the positive or negative *z*-axis. This orientation significantly alters the SW dispersion relation, which in turn impacts SAW absorption. This inherent variability allows for diverse device configurations to manipulate both the amount of absorption and the frequency band of its occurrence. Once programmed via a variable external magnetic field or spin torque methods[28], the islets maintain a stable magnetic state, requiring only a constant bias field to facilitate magnetoelastic interaction. This would reduce both size and energy requirements significantly compared to existing field-tuned solutions, while offering similar capabilities.

We compare two device configurations: the A-state, where adjacent islets have antiparallel magnetic moments, and the P-state, where they are parallel. In the A-state, stray fields form flux closures, which enhance the internal magnetic fields within the islets. This increases the system's stiffness and, consequently, its resonance frequencies compared to islets in the P-state, where magnetic field lines repel. Therefore, we anticipate a shift in the SW dispersion relation between the P- and A-states, leading to differences in SAW absorption, which we test using the Rayleigh SAW mode as an example.

Results

Micromagnetics

In order to explore the feasibility of the proposed device, we make use of micromagnetism, which enables the simulation of spatially varying magnetization patterns, a crucial requirement due to the islet-based architecture of the device. The equation of motion of the magnetization vector is given by the Landau-Lifshitz-Gilbert equation (LLG)[29,30]

$$\frac{\mathrm{d}\,\boldsymbol{m}}{\mathrm{d}\,t} = \frac{-\gamma}{1+\alpha^2}\left[\boldsymbol{m}\times\boldsymbol{H}_{\mathrm{Eff}} + \alpha\boldsymbol{m}\times\left(\boldsymbol{m}\times\boldsymbol{H}_{\mathrm{Eff}}\right)\right], \tag{1}$$

where $\gamma = \mu_0\gamma_e$ is the reduced gyromagnetic ratio with the vacuum permeability μ_0, $\boldsymbol{m} = \boldsymbol{M}/M_{\mathrm{s}}$ is the reduced magnetization with the saturation magnetization M_{s}, and α is the Gilbert damping. The effective field $\boldsymbol{H}_{\mathrm{eff}}$ is given by the negative variational derivative of the total magnetic energy E_{M} with respect to the magnetic polarization. E_{M} can be comprised of several energy contributions in the magnetic region(s) Ω, such as the Zeeman energy under an external field $\boldsymbol{H}_{\mathrm{ext}}$, stray-field energy with demagnetization field $\boldsymbol{H}_{\mathrm{dem}}$, exchange energy with exchange stiffness A_{ex}, and uniaxial magnetic anisotropy with strength K_{u} along the easy axis $\boldsymbol{e}_{\mathrm{u}}$[31]. To describe the interaction of the SAW with the magnetic islets of the device, E_{M} also has to include a magneto-elastic energy term E_{MagEl}, describing the coupling of the normalized magnetization $\boldsymbol{m}$ with the displacement of the material $\boldsymbol{u}$. This term is given by[32–35]

$$E_{\mathrm{MagEl}} = \frac{1}{2}\int_{\Omega}\left(\boldsymbol{\varepsilon}-\boldsymbol{\varepsilon}_{\mathrm{m}}\right) : C : \left(\boldsymbol{\varepsilon}-\boldsymbol{\varepsilon}_{\mathrm{m}}\right)\,\mathrm{d}\boldsymbol{x} \tag{2}$$

$$\varepsilon_{ij} = \frac{1}{2}\left(\frac{\partial u_i}{\partial x_j}+\frac{\partial u_j}{\partial x_i}\right) \tag{3}$$

$$\varepsilon_{\mathrm{m},ij} = \begin{cases} \frac{3}{2}\lambda_{\mathrm{s}}(m_i^2-\frac{1}{3}) & i=j \\ \frac{3}{2}\lambda_{\mathrm{s}}m_i m_j & i\neq j \end{cases} \tag{4}$$

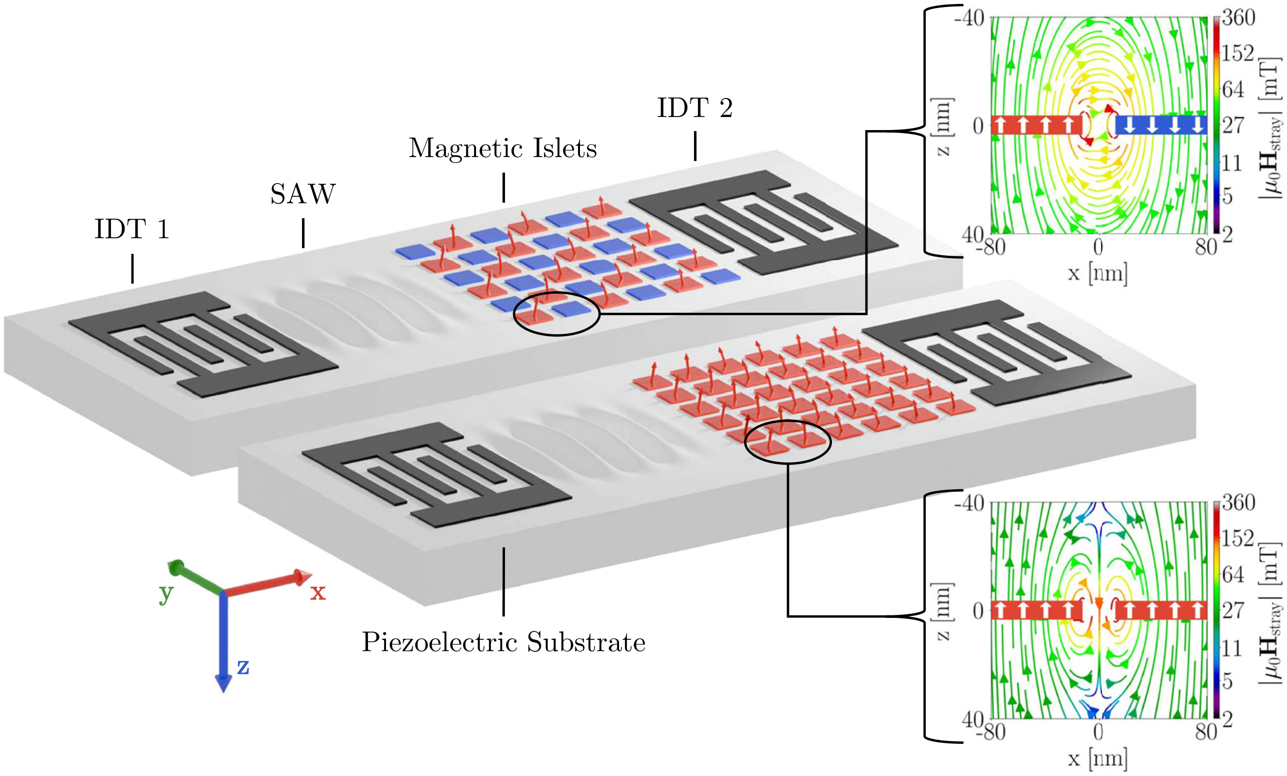

Fig. 1 | Illustration of the proposed device in antiparallel configuration (top) and parallel configuration (bottom). Insets show cross-sections of the stray fields between neighboring islets. Some simplifications were made in this depiction to show the principal functionality of the device more clearly: a reduction in the number of islets and an increase in their size, exaggeration of SAW amplitude, the omission of the capping layer and constant external bias field, as well as assuming a homogeneous magnetization of the islets.

where C is the stiffness tensor, λ_s the saturation magnetostriction, $\boldsymbol{\varepsilon}$ the strain associated with the displacement, $\boldsymbol{\varepsilon}_m$ the strain associated with the local magnetization and ":" denotes the Frobenius inner product. In Eq. (4), a polycrystalline material with at least cubic symmetry was assumed. E_M and $\boldsymbol{H}_{eff}$ can then be expressed by

$$\begin{aligned} E_M \quad = \quad & \int_\Omega -\mu_0 M_s \boldsymbol{m} \cdot \left[\boldsymbol{H}_{Ext} + \frac{1}{2}\boldsymbol{H}_{dem}\right] \\ & + A_{ex} \sum_{i,j} \left(\frac{\partial m_i}{\partial x_j}\right)^2 - K_u \left(\boldsymbol{m} \cdot \boldsymbol{e}_u\right)^2 \\ & + \frac{1}{2}\left(\boldsymbol{\varepsilon} - \boldsymbol{\varepsilon}_m\right) : C : \left(\boldsymbol{\varepsilon} - \boldsymbol{\varepsilon}_m\right) \, \mathrm{d}\boldsymbol{x} \end{aligned} \tag{5}$$

$$\boldsymbol{H}_{eff} = -\frac{1}{\mu_0 M_s} \frac{\delta E_M}{\delta \boldsymbol{m}}. \tag{6}$$

Self-consistent solvers, capable of simulating the coupled magnetic and mechanical dynamics from initial and boundary conditions of the magnetization, displacement, and momentum, can be found in ref. 35 for finite-element models and refs. 36,37 for finite-difference models. However, these self-consistent approaches are computationally intensive. This is because they need to solve multiple coupled differential equations each timestep. Crucially, they must also simulate large parts or even the entire substrate. Because the substrate is often significantly thicker than the magnetic region, this can increase the system size by multiple orders of magnitude, leading to substantially increased simulation times.

Uni-directional model

To mitigate this problem and efficiently calculate the magnetic transmission losses ΔS_{ij} of a SAW signal due to interaction with the magnetic islets of the device, we augment the macrospin model developed in refs. 20,21,38 with micromagnetic simulations performed with the finite-difference Python library magnum.np[39]. This hybrid model was validated on experimental results from ref. 26. The validation, as well as the full derivation of the model, can be found in the "Methods" section. A short overview of the working principle is given here:

The losses ΔS_{ij} in decibels are given by

$$\Delta S_{ij} = 10\log_{10}\left(\frac{P_{out}}{P_{in}}\right), \tag{7}$$

where P_{in} and P_{out} are the SAW power before and after interaction with the device, respectively. Note that ΔS_{ij} only takes into account the magnetoelastic interaction and disregards other contributions to the total transmission losses S_{ij}. In the model, the displacement $\boldsymbol{u}$ drives magnetization processes as part of the LLG according to Eq. (1)–(6). However, the energy the SAW loses to the magnetic system during this process is assumed to result solely in a decay of its amplitude, which gets estimated from an energy conservation argument. The magnetic system gains energy in this way until an equilibrium is reached, where the energy pumped into the system by the SAW equals the energy lost due to Gilbert damping.

Unlike macrospin-based magneto-elastic models[20,21,38], this approach is capable of predicting the results even for complex magnetization textures like the islet design, as no analytical solutions for the spin wave dynamics have to be provided. Namely, given the parameterization of some SAW mode with velocity c, we simulate the rate of energy transfer from the elastic into the magnetic system, R_T, over a few periods of the SAW until this energy flow becomes constant ($\frac{\mathrm{d}}{\mathrm{d}t} R_T = 0$). From this value and the total SAW energy E_{Ph}, obtained in a pre-simulation step, we can estimate the spatial rate for the energy loss of the SAW, allowing us to determine ΔS_{ij} for a signal that has traversed the islet pattern of length l:

$$\Delta S_{ij}(l) = \frac{10}{\ln(10)} \frac{l}{c} \frac{-R_T}{E_{Ph}} \tag{8}$$

$$R_T = -\int_\Omega \left(\frac{\partial}{\partial t}\boldsymbol{\varepsilon}\right) : C : \boldsymbol{\varepsilon}_m \, \mathrm{d}\boldsymbol{x} \tag{9}$$

$$E_{Ph} = \frac{1}{2}\int_V \boldsymbol{\varepsilon} : C : \boldsymbol{\varepsilon} + \rho v^2 \, \mathrm{d}\boldsymbol{x}. \tag{10}$$

Here, V is the volume of the simulated section, Ω is the magnetic region(s) of that volume, ρ is the material density, and $\boldsymbol{v} = \frac{\mathrm{d}\boldsymbol{u}}{\mathrm{d}t}$. Because only R_T has to be determined in simulation, but vanishes outside Ω, this reduces the computational complexity from 3D to quasi-2D for thin magnetic structures, as is the case with the islet design, leading to a significant increase in computational speed.

Material parameters and device geometry

Co/Ni multilayer structures were identified as a possible material candidate for the magnetic islets of the programmable device. They have shown OOP uniaxial magnetic anisotropy, a sizable magnetic moment[40–42], which is necessary in order to maximize the stray-field interaction between the islets themselves, and a moderate Gilbert damping[41,42]. The parameters used in this section are based on a Ta(3 nm)/Pt(20 nm)/[Co(0.4 nm/Ni(0.3 nm)]$_{10}$/ Ta(3 nm)/Pt(3 nm) film studied in ref. 40. While the magnetostriction coefficient λ_s, necessary to facilitate efficient phonon-magnon coupling, was not measured in ref. 40, similar multilayer structures have shown substantial λ_s values[43]. λ_s, as well as other properties not directly available in the literature, were estimated from the individual bulk values of the materials. The parameters used for the simulation of the magnetic Co/Ni multilayer are given in Table 1[40–42,44–48]. To prevent the islets from coupling via exchange interaction, we separate them with a demagnetized spacer material where $A_{ex} = \boldsymbol{m} = K_u = 0$. To simplify the model, we assume the mechanical properties of both spacings and islets to be identical and isotropic. Depending on how the spacings are realized experimentally (see sec. "Experimental feasibility"), they could influence the SAW mode, however.

Here, E is the Young modulus and v the Poisson ratio. The uniaxial magnetic anisotropy K_u along the OOP direction is larger than the thin film shape anisotropy ($\frac{1}{2}\mu_0 M_s^2$), giving rise to an effective OOP easy axis direction.

Each islet has a size of 200 × 200 × 36 nm^3, with a spacing of 25 nm between them and is placed on a 36°-rotated Y-cut X-propagation LiTaO$_3$ substrate. We investigate two distinct configurations of these islets (see Fig. 2): A 1D device designed to characterize the behavior of islets situated atop a waveguide and a 2D device representative of a conventional SAW filter. Due to the increased number of neighbors in the 2D device, we expect the shift in dispersion relation to be more pronounced compared to the 1D case. Possible avenues for the experimental realization of the device are discussed in the "Methods" section.

To model these configurations, islets are arranged in a line and periodic boundary conditions (PBCs) in the x direction are applied for the 1D device, whereas for the 2D device, they are arranged in an $n \times 2$ grid with PBCs in both the x and y directions. The application of PBCs is essential for accurate

Table 1 | Assumed material parameters used for the simulation of the magnetic Co/Ni multilayer, based on a Ta(3 nm)/ Pt(20 nm)/[Co(0.4 nm/Ni(0.3 nm)]$_{10}$/ Ta(3 nm)/Pt(3 nm) film[40–42,44–48]

A_{ex}	M_s	K_u	α	λ_s	ρ	E	v
[pJ/m]	[kA/m]	[kJ/m^3]	[1]	[10^{-6}]	[kg/m^3]	[GPa]	[1]
10	725	366	0.05	-51.71	9141	270.7	0.263

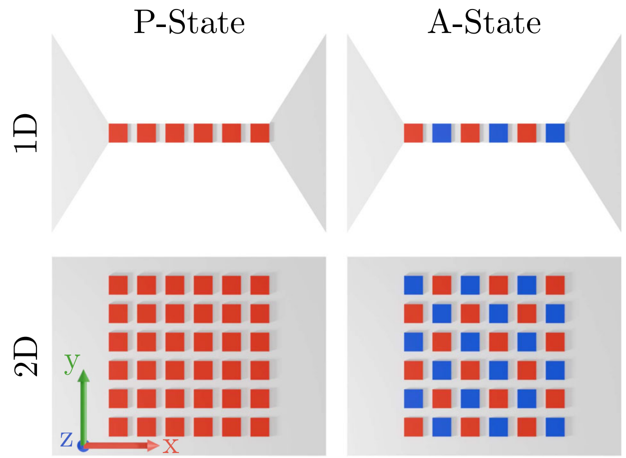

Fig. 2 | Illustration of the studied islets in parallel (P) and antiparallel (A) configurations in a 1D and 2D device. Red signifies a magnetization pointing OOP away from the substrate, blue into the substrate.

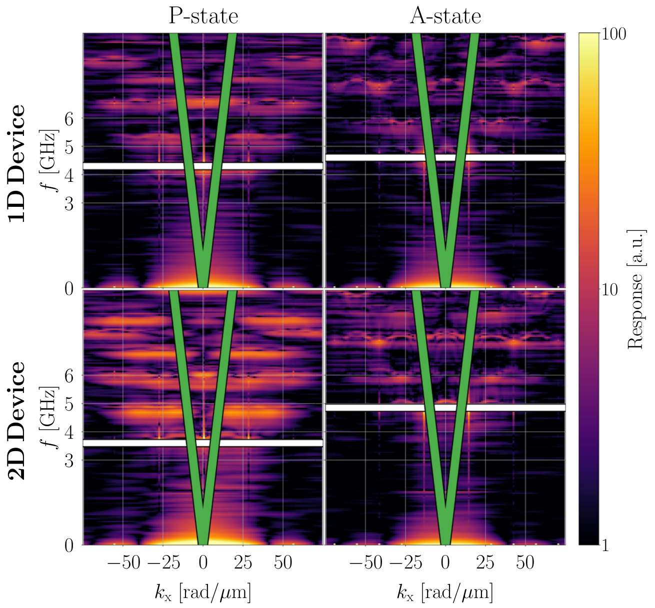

Fig. 3 | Magnetization dynamics response of the 1D and 2D devices described in section “Material parameters and device geometry” in the P- and A-states to a magnetic sinc pulse under the influence of a 50 mT bias field along the x direction. The scales of the plot were limited to the range of 1 to 100 to emphasize the relevant data. The linear SAW dispersion relation for $c = 3068.2$ m/s is overlaid as a green line. The frequencies where the SAW dispersion intersects the first-order SW dispersion are highlighted by white lines: 4.30 GHz and 4.60 GHz for the P- and A-states, respectively, of the 1D device; 3.60 GHz and 4.85 GHz for the 2D device.

device modeling, as it mitigates finite-size effects of the stray field, thereby enabling the simulation of the whole device from a much smaller subregion. For both devices, the discretization of the simulation geometry is (5 nm, 5 nm, $\frac{7}{4}$ nm) when simulating magnetization dynamics, where only the 7 nm thick Co/Ni multilayer is considered.

Dispersion relation

In order to quickly evaluate different sets of material parameters and geometries regarding their programmability, we calculate the spin wave dispersion for the parallel and antiparallel states. We employ the methodology proposed in ref. 49, where a magnetic sinc-pulse $\boldsymbol{h}_{\mathrm{excite}}$ in space and time is used to excite all possible SW modes at once. In addition, the OOP uniaxial magnetic anisotropy K_{u}, a constant bias field $\mu_0 H_{\mathrm{ext}} = 50$ mT applied along the x-axis and the demagnetization and exchange energies are considered. The external field will later be necessary to facilitate efficient magneto-phononic coupling, because the main strain components of the Rayleigh SAW mode, ε_{xx} and ε_{zz}, favor an equilibrium magnetization which is tilted towards the x-axis[50]. Additionally, the field is used to shift the spin wave dispersion into a desired frequency range, with higher fields leading to lower resonance frequencies. It could be provided by a bias magnet in an experimental realization.

In this simulation, the 1D and 2D magnetic islet patterns are 24 islets long (5.4 μm). First, they are relaxed using a Gilbert damping α of 1 and without $\boldsymbol{h}_{\mathrm{excite}}$. Due to the demagnetization energy and the external bias field, the equilibrium magnetization of the islets is not homogeneous. While the magnetization at the edges of the islets remains mostly parallel to the z-axis, the x-component of the magnetization increases towards the islet center with the polar angle depending on the device and state. For the parameters described in sec. Material Parameters and Device Geometry, the polar angle at the islet center is ≈ 20.0° and ≈ 21.5° for the A- and P-states of the 1D device, respectively, and ≈ 19.5° and ≈ 24.0° for the A- and P-states of the 2D device.

The simulation is then performed for 20 ns with 1 ps integration steps and $\alpha = 10^{-8}$. The Gilbert damping was set close to zero in order to sharpen the dispersion relation. During this, the magnetization gets saved for each time step, from which the dispersion relation gets calculated via a Fast Fourier Transform. The simulation results for the devices described in section “Material parameters and device geometry” are presented in Fig. 3: The islet pattern magnonic crystal[51] shows a complicated discretized dispersion relation which largely differs for the P- and A-states. As expected, the shift in the SW dispersion for the 2D device (1.25 GHz) is larger than that of the 1D device (0.3 GHz). We attribute the quite broad resonances to both stray fields and equilibrium magnetization not being homogeneous across the islet.

SAW parameterization

While LiTaO$_3$ can support both shear horizontal and Rayleigh SAW modes[52], this study will focus on the Rayleigh mode. Because this mode exhibits non-vanishing displacement both in the direction of travel and transversal to it[53], it has a sense of rotation, leading to a non-reciprocal absorption of the SAW depending on the direction of travel under an external field[21,26]. This non-reciprocity will be used to validate the unidirectional model in the “Methods” section.

Using the convention of a z-axis which starts at the surface and points into the device, a parameterization of the Rayleigh mode is given in ref. 54 as:

$$\boldsymbol{u} = A \frac{\widetilde{\boldsymbol{u}}}{\max\left(|\widetilde{\boldsymbol{u}}|\right)} \tag{11}$$

$$\begin{aligned} \widetilde{u}_{\mathrm{x}}(x,z,t) \;&=\; \kappa_{\mathrm{t}} \cos\left(kx - \omega t\right) \\ &\cdot \left[\exp\left(-\kappa_{\mathrm{t}} z\right) - \tfrac{2k^2}{k^2+\kappa_{\mathrm{t}}^2} \exp\left(-\kappa_{\mathrm{l}} z\right)\right] \end{aligned} \tag{12}$$

$$\widetilde{u}_{\mathrm{y}}(x,z,t) = 0 \tag{13}$$

$$\begin{aligned} \widetilde{u}_{\mathrm{z}}(x,z,t) \;&=\; -k \sin\left(kx - \omega t\right) \\ &\cdot \left[\exp\left(-\kappa_{\mathrm{t}} z\right) - \tfrac{2\kappa_{\mathrm{t}}\kappa_{\mathrm{l}}}{k^2+\kappa_{\mathrm{t}}^2} \exp\left(-\kappa_{\mathrm{l}} z\right)\right] \end{aligned} \tag{14}$$

where A is the amplitude of the SAW, with κ_{l} and κ_{t} being the longitudinal- and transversal penetration components. They depend on the angular frequency ω and wave number k of the SAW, as well as the longitudinal- and transversal velocities v_{l} and v_{t}:

$$\kappa_{\mathrm{l}} = \sqrt{k^2 - \frac{\omega^2}{v_{\mathrm{l}}^2}} \tag{15}$$

Table 2 | SAW parameters

c [m/s]	v_l [m/s]	v_t [m/s]	A_0 [pm]
3068.2	5312.4	3398.3	4.00

$$\kappa_t = \sqrt{k^2 - \frac{\omega^2}{v_t^2}}. \tag{16}$$

These equations were derived for a single isotropic material. However, we assume they still model the full device well, because the islets' thickness of 36 nm is significantly lower than the employed SAW wavelengths (511 nm to 1023 nm), resulting in the majority of the SAW energy being confined to the substrate rather than the islets. The dispersion relation is then given by[55]

$$\omega = v_t \xi k, \tag{17}$$

where we identify $v_t\xi$ to be the velocity c of the SAW with ξ being the positive, real valued solution of the governing equation[55]

$$\xi^6 - 8\xi^4 + 8\xi^2\left(3 - 2\frac{v_t^2}{v_l^2}\right) - 16\left(1 - \frac{v_t^2}{v_l^2}\right) = 0. \tag{18}$$

To determine v_t and v_l, a finite-element simulation of the layered system was carried out using COMSOL®[56] at f = 3.07 GHz where the resulting depth profile of $\boldsymbol{u}(\boldsymbol{x}, t)$ was fitted to Eq. (12) and (14). $\boldsymbol{u}(\boldsymbol{x}, t)$ is thus parametrized by the values in Table 2 for Eq. (11) to (18). Small frequency-dependent changes in c were neglected, and A_0 was chosen such that it is large enough to minimize numerical errors, while also being small enough to stay in the linear regime of the LLG. For material parameters similar to the ones employed here, the validity range of A_0 is approximately 10^{-15} m to 10^{-10} m. Furthermore, the modeling assumes weak coupling, as observed in experiments for similar continuous magnetic films[21,26].

Magneto-phononic interaction

To calculate the SAW transmission of our devices, we sequentially excite them with SAWs between 3 GHz and 6 GHz. The frequencies used, f_{SAW}, were chosen such that n of their corresponding wavelengths (ranging from 511 nm to 1023 nm) are equal to $2m$ islets and spacings, where n and m are integers:

$$n\frac{c}{f_{\mathrm{SAW}}} = 2m \cdot (200\,\mathrm{nm} + 25\,\mathrm{nm}). \tag{19}$$

This is necessary to ensure that PBCs can be used. The simulated section of the magnetic pattern then consists of $2m$ islets and buffers. Note that this section can be much smaller than the total length of the islet pattern (≈ 1 mm). For each design, configuration, and frequency, the following procedure was then repeated: The initial magnetization configuration of the islets was set along the OOP axis and neighboring islets are initialized either with parallel or antiparallel magnetization, depending on the state of the device, after which this state was relaxed at $\alpha = 1$ under the influence of (i) demagnetization energy, (ii) exchange energy with stiffness A_{ex}, (iii) OOP uniaxial anisotropy with strength K_u and (iv) Zeeman energy of a 50 mT external field along the x-axis. For the simulations themselves, $\alpha = 0.05$ was set, and the (v) magneto-elastic energy with saturation magnetization λ_s was added to energy terms (i) to (iv). Then, the SAW was activated, and the simulation proceeded with a time discretization of $\Delta t = \frac{1}{50 f_{\mathrm{SAW}}}$. At each time step, ΔS_{21} was calculated according to Eq. (8) for a 1 mm long islet pattern where E_{Ph} was determined in a pre-simulation step using COMSOL®[56] and scaled according to $E_{\mathrm{Ph}} \propto f$. The simulation concludes when, for 50 consecutive time steps (one period of the SAW), the relative change in ΔS_{21} is less than 10^{-5} or its absolute change is less than 10^{-3} dB:

$$\left|\frac{\Delta S_{21}(t) - \Delta S_{21}(t - \Delta t)}{\Delta S_{21}(t)}\right| < 10^{-5} \tag{20}$$

$$\left|\Delta S_{21}(t) - \Delta S_{21}(t - \Delta t)\right| < 10^{-3}\,\mathrm{dB}. \tag{21}$$

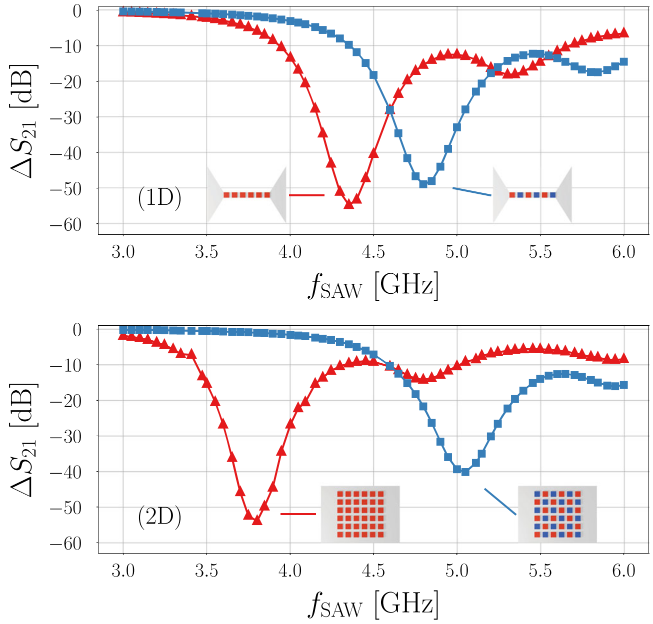

Fig. 4 | Simulation results for the transmission losses due to the magnon-phonon interaction, ΔS_{21}, after 1 mm travel distance in the 1D (top) and 2D (bottom) devices at different frequencies of the SAW in different magnetic states: parallel (red triangles) and antiparallel (blue squares). Insets show illustrations of the different islet arrangements. Simulations were performed under the influence of a 50 mT bias field along the x direction.

This convergence criterion, while equivalent to requiring a constant energy flow because $\Delta S_{21} \propto R_T$, is better suited for practical applications. The final ΔS_{21} value is then determined by averaging ΔS_{21} over these 50 time steps to further mitigate numerical noise.

In the simulated section of the magnetic pattern (with a length of $2m$ islets and buffers), we set $A(x) = A_0 = const.$ This is necessary because it allows the use of PBCs. Nevertheless, this introduces a small error to the calculation, because the SAW attenuation in this small section slightly changes $\frac{\partial \boldsymbol{u}}{\partial x}$ and thus $\boldsymbol{\varepsilon}$. However, this error is negligible when the decay of $A(x)$ within one wavelength of the SAW is small, as is the case there. The transmission efficiency itself is independent of the choice of A, as only the ratio between R_T and E_{Ph} is relevant for its calculation (Eq. (8)), and both are proportional to A^2 in the linear regime of the LLG.

At f_{SAW} = 4.546 GHz, where the SAW wavelength is an integer multiple of the periodicity of the islets ($\lambda = \frac{3068.2\,\mathrm{m/s}}{4.546\,\mathrm{GHz}} = 3 \cdot 225\,\mathrm{nm}$), conditions from Eqs. (20) or (21) were not met within 10ns of simulation time for any device or configuration. Similarly, for f_{SAW} = 3.409 GHz, where $\lambda = \frac{3068.2\,\mathrm{m/s}}{3.409\,\mathrm{GHz}} = 4 \cdot 225\,\mathrm{nm}$, the A-state of the 1D device did not converge (the other three simulations at that frequency did, however). For all five of these simulations, the instantaneous ΔS_{21} values oscillated slightly (<0.4 dB at 4.546 GHz and ≈ 1.6 dB at 3.409 GHz) around a constant value, where that value would be consistent with those of the surrounding frequencies. These simulations were nevertheless not included in the results. We attribute this to higher-order harmonics also being excited by the SAW, which only get damped when their periodicity does not match that of the islets.

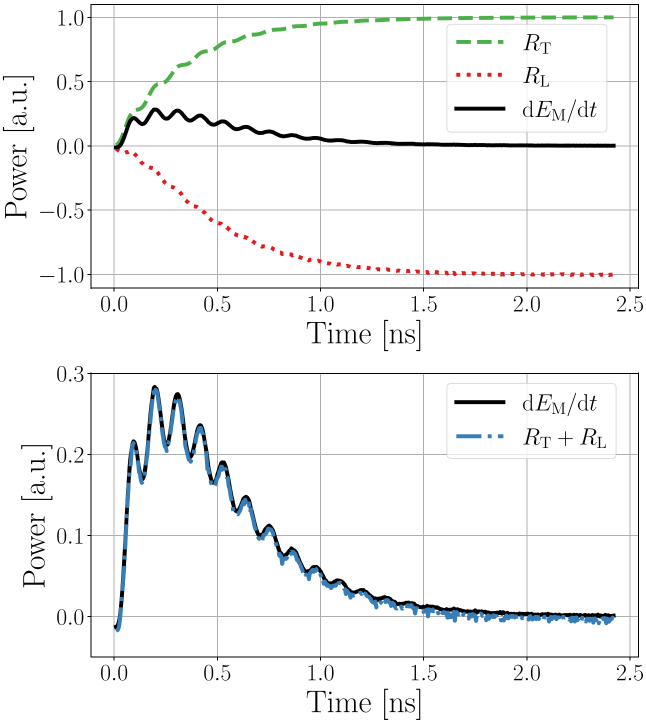

Fig. 5 | Example simulation of the magneto-phononic interaction within a thin magnetic film under the influence of an external field. The system was in energetic equilibrium when, at $t = 0$ a continuous SAW signal was launched. The top graph shows the dissipative losses of the magnetic system (Eq. (24)) in red, the energy transferred from the phonon to the magnon (Eq. (25)) in green and the total change in energy in black, (approximated via $\frac{\mathrm{dE_M}}{\mathrm{dt}}(\mathrm{t}) \approx \frac{\mathrm{E_M(t+\Delta t)-E_M(t-\Delta t)}}{2\Delta\mathrm{t}}$). At $t = 2.43$ ns, the convergence criterion was reached. The bottom graph shows the validity of Eq. (23) with $R_\mathrm{T} + R_\mathrm{L}$ (blue) indeed summing to $\frac{\mathrm{d}E_\mathrm{M}}{\mathrm{d}\,t}$ (black).

Interpretation

Figure 4 shows the transmission losses ΔS_{21} of the SAW resulting from magnon-phonon interaction in both 1D and 2D devices, under parallel and antiparallel configurations. A notable shift in the location of the transmission dips is observed in the 1D and 2D devices (0.45 GHz and 1.25 GHz, respectively), which largely correlates with the SW resonance modes presented in Fig. 3, albeit at slightly higher frequencies than predicted. This deviation is attributed to both the broad response observed from the sinc pulse excitation as well as the islets not being homogeneously magnetized. The smaller transmission dips appearing at higher frequencies (e.g. 4.80 GHz and 5.95 GHz for the 2D P-state) are also in agreement with the detected SW modes between 3 GHz and 6 GHz in Fig. 3. Importantly, significant differences in SAW attenuation between the states are observed, which is optimized for our 2D device at 3.80 GHz, with $\Delta S_{21} = -$ 54.0 dB/mm in the P-state and only -2.0 dB/mm in the A-state.

While the presented results are purely theoretical, all material parameters and geometries were chosen such that an experimental implementation should be feasible (see section "Experimental feasibility"). Furthermore, we hypothesize the existence of configurations that allow for frequency absorption at points between simple parallel alignment or perfect checkerboard arrangements. If achievable, integrating this functionality with chirped IDTs, which are capable of exciting a broad range of frequencies rather than a single one[57], would facilitate the development of a millimeter-sized RF notch filter with arbitrary frequency selectivity.

Discussion

In this study, we have demonstrated the theoretical viability of a magneto-phononic device concept capable of switching SAW attenuation at a target frequency solely depending on its internal magnetic configuration. The shift in the SW dispersion relation resulting from the stray-field interactions of the parallel vs antiparallel aligned magnetic Co/Ni islets making up the device was shown to be significant enough to alter the SAW attenuation by as much as 52.0 dB/mm between them.

The algorithm developed to carry out these simulations was successfully validated on the results presented in ref. 26, showing that the assumptions made in its derivation are reasonable. Furthermore, due to the reduction in computational complexity by this approach, it is possible to sweep through a very large set of simulation parameters in a reasonable amount of time while maintaining great accuracy.

Methods

Uni-directional model: derivation

The principal assumptions of the model are:

- The SAW only loses energy through a reduction in its amplitude A. While it is known that the SAW velocity can change due to the magneto-phononic interaction, the relative change is typically limited to <1%[58–60]. As we want to calculate the magnetic transmission losses ΔS_{ij}, where relative changes can reach ≈100%, we neglect these small changes in c. In systems where a significant change in c is expected, this would need to be incorporated in the model.
- Similarly, magneto-rotational coupling[59–61] is also not incorporated into our model, as its contributions are small when the saturation magnetostriction λ_s is large (see Supplementary Information for details).
- Measurements are only taken once the system is in a state of constant energy flow between the mechanical and magnetic systems ($\frac{\mathrm{d}R_\mathrm{T}}{\mathrm{d}\,t} = 0$). This can only occur for a sustained SAW signal of at least a couple of periods (see Fig. 5).

We start by examining the total change in energy of the magnetic system $\frac{\mathrm{d}E_\mathrm{M}}{\mathrm{d}\,t}$:

$$\frac{\mathrm{dE_M}}{\mathrm{dt}} = \int_\Omega \frac{\mathrm{d}}{\mathrm{d}t} U_\mathrm{M}(t, \boldsymbol{m}(t)) \;\; \mathrm{d}\boldsymbol{x} \tag{22}$$

$$= \underbrace{\int_\Omega \frac{\delta U_\mathrm{M}(t, \boldsymbol{m}(t))}{\delta \boldsymbol{m}} \frac{\mathrm{d}\boldsymbol{m}}{\mathrm{dt}} \mathrm{d}x}_{\equiv R_L} + \underbrace{\int_\Omega \frac{U_\mathrm{M}(t, \boldsymbol{m}(t))}{t} \mathrm{d}x}_{\equiv R_T}. \tag{23}$$

Here, U_M denotes the magnetic energy density, and R_L are the dissipative losses due to Gilbert damping with the well-known result[31]

$$R_\mathrm{L} = -\frac{\alpha\gamma}{1+\alpha^2}\mu_0 M_\mathrm{s} \int_\Omega (\boldsymbol{m} \times \boldsymbol{H}_\mathrm{Eff})^2 \;\mathrm{d}\boldsymbol{x}. \tag{24}$$

For R_T, we make use of the fact that, for constant H_ext, the magneto-elastic energy term (Eq. (2)) is the only one that explicitly depends on time in E_M. When the simulation geometry is an integer multiple of the wavelength, $\int_\Omega \frac{\partial}{\partial t}(\boldsymbol{\varepsilon} : C : \boldsymbol{\varepsilon}) \;\mathrm{d}\,\boldsymbol{x} = 0$. Given that $\boldsymbol{\varepsilon}_\mathrm{m}$ has no explicit time dependence, $\frac{\partial \boldsymbol{\varepsilon}_\mathrm{m}}{\partial t} = 0$. Thus, for a symmetric C, R_T simplifies to

$$R_\mathrm{T} = -\int_\Omega \left(\frac{\partial \boldsymbol{\varepsilon}}{\partial t}\right) : C : \boldsymbol{\varepsilon}_\mathrm{m} \;\mathrm{d}\boldsymbol{x}. \tag{25}$$

Using the law of energy conservation, we know that all energy gained by the magnetic system has to be compensated by a loss in the energy of the phonon, E_Ph:

$$\frac{\mathrm{d}E_\mathrm{Ph}}{\mathrm{d}t} = -R_\mathrm{T} = \int_\Omega \left(\frac{\partial}{\partial t}\boldsymbol{\varepsilon}\right) : C : \boldsymbol{\varepsilon}_\mathrm{m} \;\mathrm{d}\boldsymbol{x}. \tag{26}$$

If the magneto-phononic interaction is weak enough that the LLG stays in a linear regime, it is known that E_Ph follows an exponential decay[21,26] (in the Supplementary Information, a possible extension of this approach to the non-linear regime is discussed):

$$E_{\mathrm{Ph}}(t) = E_{\mathrm{Ph}}(0)e^{\beta t}. \tag{27}$$

Using Eq. (26), we can express the decay rate β as

$$\beta = \beta\frac{E_{\mathrm{Ph}}(0)e^{\beta t}}{E_{\mathrm{Ph}}(0)e^{\beta t}} = \frac{1}{E_{\mathrm{Ph}}(t)}\frac{\mathrm{d}E_{\mathrm{Ph}}}{\mathrm{d}t}(t) = \frac{-R_{\mathrm{T}}(t)}{E_{\mathrm{Ph}}(t)} \tag{28}$$

where we can see, that it is sufficient to know R_{T} and E_{Ph} for any single point in time, in order to obtain β for the full interaction. R_{T} can be calculated from Eq. (25), where we simulate a segment of the magnetic material until R_{T} becomes constant (see Fig 5). E_{Ph} can be obtained in a pre-simulation step by summing the potential energy $\frac{1}{2}\boldsymbol{\varepsilon} : C : \boldsymbol{\varepsilon}$ and kinetic energy $\frac{\rho v^2}{2}$ of the SAW over the full volume V, including possible non-magnetic layers[55]:

$$E_{\mathrm{Ph}} = \frac{1}{2}\int_V \boldsymbol{\varepsilon} : C : \boldsymbol{\varepsilon} + \rho\boldsymbol{v}^2 \ \mathrm{d}\boldsymbol{x}. \tag{29}$$

Given that both $\boldsymbol{\varepsilon}$ and $\boldsymbol{v}$ are derived from $\boldsymbol{u}$, they are proportional to A and therefore: $E_{\mathrm{Ph}} \propto A^2$. Using $P \propto A^2$[62], where P is the power of the SAW, we find:

$$P \propto E_{\mathrm{Ph}}. \tag{30}$$

Finally, by viewing the phonon as a quasi-particle with a position $x(t) = ct$, where $c = v_t\xi$ is its velocity, we can give its energy in terms of its position instead of time:

$$E_{\mathrm{Ph}}(t) = E_{\mathrm{Ph}}\left(\frac{x(t)}{c}\right). \tag{31}$$

Combining Eq. (26) to (31), we obtain the magnetic transmission losses ΔS_{ij} by setting the position of the phonon $x(t)$ to the length of the magnetic material l:

$$\Delta S_{ij}(l) = 10\log_{10}\left(\frac{P_{\mathrm{out}}}{P_{\mathrm{in}}}\right) \tag{32}$$

$$= 10\log_{10}\left(\frac{E_{\mathrm{Ph}}(l/c)}{E_{\mathrm{Ph}}(0)}\right) \tag{33}$$

$$= 10\log_{10}\left(\exp\left(\frac{l}{c}\beta\right)\right) \tag{34}$$

$$= \frac{10}{\ln(10)}\frac{l}{c}\beta \tag{35}$$

$$= \frac{10}{\ln(10)}\frac{l}{c}\frac{-R_{\mathrm{T}}}{E_{\mathrm{Ph}}} \tag{36}$$

$$= \frac{10}{\ln(10)}\frac{l}{c}\frac{\int_\Omega\left(\frac{\partial}{\partial t}\boldsymbol{\varepsilon}\right) : C : \boldsymbol{\varepsilon}_{\mathrm{m}} \ \mathrm{d}\boldsymbol{x}}{\frac{1}{2}\int_V \boldsymbol{\varepsilon} : C : \boldsymbol{\varepsilon} + \rho\boldsymbol{v}^2 \ \mathrm{d}\boldsymbol{x}}. \tag{37}$$

Uni-directional model: validation

To validate the model, we utilize material parameters from ref. 26, derived from both experimental measurements and fitting procedures. These parameters characterize a layered system comprising a 10 nm Ni thin film deposited on a $\mathrm{LiTaO_3}$ substrate, capped with a 5 nm Al layer (see Fig. 6). We then compare the simulated transmission losses of a Rayleigh SAW with corresponding experimental results. The validation procedure is largely identical to the one introduced in sec. SAW parameterization and Magneto-Phononic Interaction, only now the frequency of the SAW gets fixed at $f_{\mathrm{SAW}} = 4.47$ GHz, while the external field is varied. The following energy terms were considered: (i) demagnetization energy, (ii) exchange energy with stiffness A_{ex}, (iii) in-plane uniaxial magnetic anisotropy $K_{\mathrm{u}}^{\mathrm{IP}}$ in easy axis direction $\phi_{\mathrm{u}}^{\mathrm{IP}}$, (iv) OOP surface magnetic anisotropy counteracting the shape anisotropy $K_{\mathrm{u}}^{\mathrm{OOP}}$, (v) magneto-elastic energy with saturation magnetostriction λ_{s}, and (vi) Zeeman energy of an external field of strength H_{ext} and angle ϕ_{H}. $\phi_{\mathrm{u}}^{\mathrm{IP}}$ and ϕ_{H} are given in-plane with the x-axis. Parameters for the Ni film are taken from ref. 26 and can be seen in Table 3.

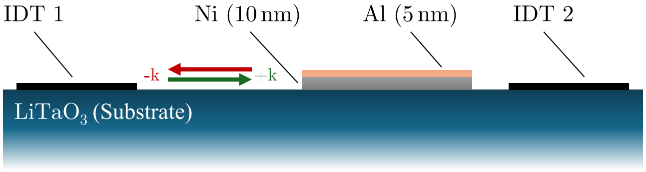

Fig. 6 | Illustrated cross-section of the device employed in ref. 26. On top of a 36°-rotated Y-cut X-propagation $\mathrm{LiTaO_3}$ substrate, two interdigital transducers (IDTs) are placed 1600 µm apart. Between them, a 1000 µm long and 10 nm thick Ni film is applied and capped with a 5 nm Al layer. $+\boldsymbol{k}$ and $-\boldsymbol{k}$ indicate the direction of SAW travel.

Table 3 | Magnetic parameters of the 10 nm thick Ni film[26]

α [1]	M_{s} [kA/m]	A_{ex} [pJ/m]	$K_{\mathrm{u}}^{\mathrm{IP}}$ [kJ/m^3]	$\phi_{\mathrm{u}}^{\mathrm{IP}}$ [°]	$K_{\mathrm{u}}^{\mathrm{OOP}}$ [kJ/m^3]	λ_{s} [10^{-6}]
0.069	408.0	7.7	0.28	83.6	23.8	−14.22

Here, $K_{\mathrm{u}}^{\mathrm{OOP}}$ was fitted, such that the peak absorption for $\phi_{\mathrm{H}} = 45°$ occurs at the same $\mu_0 H_{\mathrm{ext}}$ as the experiment (-46 mT). λ_{s} was then determined by matching simulation results for $\Delta S_{21}\left(\mu_0 H_{\mathrm{ext}} = -46\,\mathrm{mT},\ \phi_{\mathrm{H}} = 45^\circ\right)$ with the experimental value. This was done because λ_{s} was not a fit parameter in ref. 26, and $K_{\mathrm{u}}^{\mathrm{OOP}}$ was fitted in conjunction with an analytical approximation of the stray field in ref. 26, whereas the micromagnetic energy term given in Eq. (5) is used for the simulations here. Note that the fitted $K_{\mathrm{u}}^{\mathrm{OOP}}$ of 23.8 kJ/m^3 shows good agreement with the measured $K_{\mathrm{u}}^{\mathrm{OOP}}$ of 32.7 kJ/m^3 obtained from broadband ferromagnetic resonance measurements[26].

During validation, $\mu_0 H_{\mathrm{ext}}$ was varied from -72 mT to 72 mT in increments of 2 mT and ϕ_{H} from -90° to 90° in increments of 4.5° for both directions of travel of the SAW, for a total of 5986 individual simulations. For each, the system was initialized with $\boldsymbol{m}(\boldsymbol{x}) = \left(\mathrm{sgn}(H_{\mathrm{ext}})\cos(\phi_{\mathrm{H}}), \mathrm{sgn}(H_{\mathrm{ext}})\sin(\phi_{\mathrm{H}}), 0\right)$ and relaxed before the SAW was activated.

The results of this validation run can be seen in Fig. 7. The micromagnetic simulation and the experimental results show excellent agreement not only qualitatively but also quantitatively for both directions of SAW travel. The expected fourfold symmetry is clearly present, as well as the non-reciprocity between the two directions of travel. The validation took a total of ≈100 h on an NVIDIA A100 (80GB) GPU, for an average of only ≈1 minute per simulation.

Experimental feasibility

To transition the theoretical potential of this device toward practical application, we outline potential solutions for its experimental execution here.

While there are multiple possible venues to fabricate the islets, FIB seems particularly promising, as this approach has already been heavily investigated in regards of patterning a continuous thin film[63]. With this method, single-domain islands with a side length of 70 nm and a distance of 25 nm were achieved[63]. Another possibility would be to first deposit a continuous thin film, then use e-beam-lithography and reactive ion etching to pattern the film[64,65]. Here, islets had a diameter as small as 40 nm with a 60 nm gap[64].

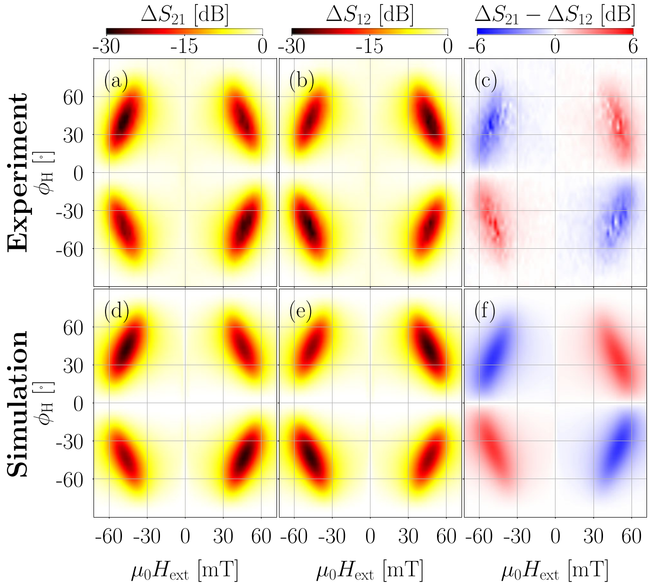

Fig. 7 | Comparison between experimental and simulation results for +k (ΔS_{21}) and -k (ΔS_{12}) SAW propagation directions. a–c Experimental results of ref. 26. **d–f** Results of micromagnetic simulations. (**a**), (**b**), (**d**), and (**e**) show the transmission losses due to the magneto-phononic interaction, while (**c**) and (**f**) give the non-reciprocity between the travel directions.

To perform a sensitivity analysis of the proposed device, we varied the following material parameters from half to double their assumed magnitude (see Table 1) in the 2D A-state, revealing the following relations: $\Delta S_{ij} \propto \lambda_s^2$, $\Delta S_{ij} \propto E^2$ and $\Delta S_{ij} \propto \frac{1}{(1+\nu)^2}$. Variations upon α led to changes in the line width of the absorption while simultaneously scaling the peaks according to $\Delta S_{ij} \propto \alpha^{-1}$. Finally, A_{ex} and K_u determine the frequency of the most efficient coupling for both P- and A-states as they shift the SW dispersion relation, while M_s influences the magnitude of the shift between these coupling frequencies.

To program the device in experiments, we suggest first saturating the islets along the z-direction, thereby achieving the P-state. Starting from this state, by applying a field in the opposite direction, we expect individual islets to start flipping due to small inhomogeneities of K_u present in a real sample. By increasing the field strength, more islands switch. Therefore, an arbitrary number of islands can be switched depending on the field strength. To achieve the A-state, every other island could be irradiated minimally in order to slightly reduce the anisotropy of these islets. We anticipate this would then lead to them flipping before the islets which were not irradiated, leading to an almost perfect checkerboard pattern.

Spin-torque methods, such as those utilized in Spin-Transfer Torque and Spin-Orbit Torque MRAM technologies[28] represent an alternative approach to programming the islets. Implementation of these techniques would likely necessitate more complex geometric structures and intricate layer stacks than those examined in the current study and are, therefore, excluded from our present scope. Nevertheless, the successful integration of spin-torque switching could facilitate dynamic, individual addressing of the magnetic islets, thereby enabling the realization of more complex magnetization patterns beyond the simple P- and A-states considered here - possibly enabling additional functionality.

Data availability

The data that support the plots presented in this paper are available from the corresponding author upon reasonable request.

Code availability

The simulation files used to generate and analyze the data are available from the corresponding author upon reasonable request.

Received: 3 September 2025; Accepted: 12 February 2026;

References

1. Morgan, D. History of saw devices. In Proceedings of the 1998 *IEEE International Frequency Control Symposium (Cat. No.98CH36165)* (IEEE, 1998).
2. Morgan, D. *Surface Acoustic Wave Filters: With Applications to Electronic Communications and Signal Processing*. In Studies in Electrical and Electronic Engineering (Academic Press, 2010).
3. Campbell, C. *Surface Acoustic Wave Devices and Their Signal Processing Applications* (Academic Press, 2012).
4. White, R. M. & Voltmer, F. W. Direct piezoelectric coupling to surface elastic waves. *Appl. Phys. Lett.* **7**, 314–316 (1965).
5. Ruppel, C., Reindl, L. & Weigel, R. Saw devices and their wireless communications applications. *IEEE Microwave Magaz*. **3**, https://doi.org/10.1109/MMW.2002.1004053 (2002).
6. Chen, P., Li, G. & Zhu, Z. Development and application of saw filter. *Micromachines* **13**, 656 (2022).
7. Liu, P. et al. Scaling LLSAW filters on engineered LiNbO3-on-SiC wafer for 5G and Wi-Fi 6 wideband applications. *Microsyst. Nanoeng.* **11**, 148 (2025).
8. Liu, Y. et al. Materials, design, and characteristics of bulk acoustic wave resonator: a review. *Micromachines* **11**, 630 (2020).
9. Yang, Y., Dejous, C. & Hallil, H. Trends and applications of surface and bulk acoustic wave devices: a review. *Micromachines* **14**, 43 (2022).
10. Delsing, P. et al. The 2019 surface acoustic waves roadmap. *J. Phys. D Appl. Phys.* **52**, 353001 (2019).
11. Mandal, D. & Banerjee, S. Surface acoustic wave (SAW) sensors: physics, materials, and applications. *Sensors* **22**, 820 (2022).
12. Ding, X. et al. On-chip manipulation of single microparticles, cells, and organisms using surface acoustic waves. *Proc. Natl Acad. Sci. USA* **109**, 11105–11109 (2012).
13. Rufo, J., Cai, F., Friend, J., Wiklund, M. & Huang, T. J. Acoustofluidics for biomedical applications. *Nat. Rev. Method. Primers* **2**, 30 (2022).
14. Webb, D., Forester, D., Ganguly, A. & Vittoria, C. Applications of amorphous magnetic-layers in surface-acoustic-wave devices. *IEEE Trans. Magnet*. **15**, https://doi.org/10.1109/TMAG.1979.1060442 (1979).
15. Yamaguchi, M., Hashimoto, K., Kogo, H. & Naoe, M. Variable saw delay line using amorphous TbFe2 film. *IEEE Trans. Magnet*. **16**, https://doi.org/10.1109/TMAG.1980.1060738 (1980).
16. Luo, B., Velvaluri, P., Liu, Y. & Sun, N.-X. Magnetoelectric baw and saw devices: a review. *Micromachines* **15**, 1471 (2024).
17. Bozhko, D. A., Vasyuchka, V. I., Chumak, A. V. & Serga, A. A. Magnon-phonon interactions in magnon spintronics (review article). *Low Temp. Phys.* **46**, 383–399 (2020).
18. Yang, W. G. & Schmidt, H. Acoustic control of magnetism toward energy-efficient applications. *Appl. Phys. Rev.* **8**, 021304 (2021).
19. Puebla, J., Hwang, Y., Maekawa, S. & Otani, Y. Perspectives on spintronics with surface acoustic waves. *Appl. Phys. Lett.* **120**, 220502 (2022).
20. Weiler, M. et al. Elastically driven ferromagnetic resonance in nickel thin films. *Phys. Rev. Lett.* **106**, 117601 (2011).
21. Dreher, L. et al. Surface acoustic wave driven ferromagnetic resonance in nickel thin films: theory and experiment. *Phys. Rev. B* **86**, 134415 (2012).
22. Li, X., Labanowski, D., Salahuddin, S. & Lynch, C. S. Spin wave generation by surface acoustic waves. *J. Appl. Phys.* **122**, 043904 (2017).
23. Casals, B. et al. Generation and imaging of magnetoacoustic waves over millimeter distances. *Phys. Rev. Lett.* **124**, 137202 (2020).
24. Kunz, Y. et al. Coherent surface acoustic wave-spin wave interactions detected by micro-focused Brillouin light scattering spectroscopy. *Appl. Phys. Lett.* **124**, 152403 (2024).

25. Yamamoto, K., Xu, M., Puebla, J., Otani, Y. & Maekawa, S. Interaction between surface acoustic waves and spin waves in a ferromagnetic thin film. *J. Magn. Magn. Mater.* **545**, 168672 (2022).
26. Küß, M. et al. Symmetry of the magnetoelastic interaction of Rayleigh and shear horizontal magnetoacoustic waves in nickel thin films on $LiTaO_3$. *Phys. Rev. Appl.* **15**, 034046 (2021).
27. Bas, D. A. et al. Nonreciprocity of phase accumulation and propagation losses of surface acoustic waves in hybrid magnetoelastic heterostructures. *Phys. Rev. Appl.* **18**, 044003 (2022).
28. Guo, Z. et al. Spintronics for energy-efficient computing: an overview and outlook. *Proc. IEEE*. **109**, https://doi.org/10.1109/JPROC.2021.3084997 (2021).
29. Lifshitz, E. M. & Landau, L. D. On the theory of dispersion of magnetic permeability in ferromagnetic bodies. *Phys. Zeitsch. der Sow.* **8**, 153 (1935).
30. Gilbert, T. L. A Lagrangian formulation of the gyromagnetic equation of the magnetic field. *Phys. Rev.* **100**, 1243 (1955).
31. Abert, C. Micromagnetics and spintronics: models and numerical methods. *Eur. Phys. J. B* **92**, 120 (2019).
32. Shu, Y. C., Lin, M. P. & Wu, K. C. Micromagnetic modeling of magnetostrictive materials under intrinsic stress. *Mech. Mater.* **36**, 975–997 (2004).
33. Zhang, J. X. & Chen, L. Q. Phase-field microelasticity theory and micromagnetic simulations of domain structures in giant magnetostrictive materials. *Acta Materialia* **53**, 2845–2855 (2005).
34. Chikazumi, S. & Graham, C. Physics of ferromagnetism 2e. In *International Series of Monographs on Physics* (OUP Oxford, 2009).
35. Liang, C. Y. et al. Modeling of magnetoelastic nanostructures with a fully coupled mechanical-micromagnetic model. *Nanotechnology* **25**, 435701 (2014).
36. Vanderveken, F. et al. Finite difference magnetoelastic simulator. *Open Res. Eur.* **1**, 35 (2021).
37. Flauger, P. et al. Modeling magnetoelastic wave interactions in magnetic films and heterostructures: a finite-difference approach. http://arxiv.org/abs/2509.06007 (2025).
38. Küß, M. et al. Nonreciprocal Dzyaloshinskii-Moriya magnetoacoustic waves. *Phys. Rev. Lett.* **125**, 217203 (2020).
39. Bruckner, F., Koraltan, S., Abert, C. & Suess, D. magnum.np: a Pytorch based GPU enhanced finite difference micromagnetic simulation framework for high level development and inverse design. *Sci. Rep.* **13**, 12054 (2023).
40. You, L., Sousa, R. C., Bandiera, S., Rodmacq, B. & Dieny, B. Co/ni multilayers with perpendicular anisotropy for spintronic device applications. *Appl. Phys. Lett.* **100**, 172411 (2012).
41. He, X. D. et al. Controllable intrinsic Gilbert damping in Pt-buffered [Co/Ni]n multilayers with enhanced perpendicular magnetic anisotropy. *J. Magn. Magn. Mater.* **519**, 167429 (2021).
42. Mizukami, S. et al. Gilbert damping in Ni/Co multilayer films exhibiting large perpendicular anisotropy. *Appl. Phys. Exp.* **4**, 013005 (2011).
43. Gopman, D. B. et al. Large Interfacial Magnetostriction in (Co/Ni)4/Pb(Mg1/3Nb2/3)O3-PbTiO3 Multiferroic Heterostructures. *ACS Appl. Mate. Interfaces* **10**, 24725–24732 (2018).
44. Klokholm, E. & Aboaf, J. The saturation magnetostriction of thin polycrystalline films of iron, cobalt, and nickel. *J. Appl. Phys.* **53**, 2661–2663 (1982).
45. Kim, K. E. & Yang, C. H. Local magnetostriction measurement in a cobalt thin film using scanning probe microscopy. *AIP Adv* **8**, 105125 (2018).
46. Project, T. M. *Materials Data on Co by Materials Project*. https://doi.org/10.17188/1186809 (U.S. Department of Energy, Office of Scientific and Technical Information, 2020); accessed Jan 14, 2025.
47. Project, T. M. *Materials Data on Ni by Materials Project*. https://doi.org/10.17188/1199153 (U.S. Department of Energy, Office of Scientific and Technical Information, 2020); accessed Jan 14, 2025.
48. Jain, A. et al. Commentary: The materials project: a materials genome approach to accelerating materials innovation. *APL Mater* **1**, 011002 (2013).
49. Venkat, G. et al. Proposal for a standard micromagnetic problem: spin wave dispersion in a magnonic waveguide. *IEEE Trans. Magnet*. **49**, https://doi.org/10.1109/TMAG.2012.2206820 (2013).
50. Küß, M. et al. Forward volume magnetoacoustic spin wave excitation with micron-scale spatial resolution. *APL Mater* **10**, 081112 (2022).
51. Krawczyk, M. & Grundler, D. Review and prospects of magnonic crystals and devices with reprogrammable band structure. *J. Phys. Condens. Matter* **26**, 123202 (2014).
52. Nakamura, K., Kazumi, M. & Shimizu, H. SH-type and Rayleigh-type surface waves on rotated Y-Cut LiTaO3. In *1977 Ultrasonics Symposium* (IEEE, 1977).
53. Sonner, M. M. et al. Ultrafast electron cycloids driven by the transverse spin of a surface acoustic wave. *Sci. Adv*. **7**, eabf7414 (2021).
54. Maekawa, S. & Tachiki, M. Surface acoustic attenuation due to surface spin wave in ferro and antiferromagnets. In *AIP Conference Proceedings*. Vol. 29, 542–543 (AIP, 1976).
55. Landau, L. D., Lifshitz, E. M., Sykes, J. B., Reid, W. H. & Dill, E. H. Theory of elasticity: Vol. 7 of course of theoretical physics. *Phys. Today* **13**, https://doi.org/10.1063/1.3057037 (1960).
56. COMSOL. COMSOL Multiphysics® v. 6.3.0.290. https://www.comsol.com (COMSOL AB, Stockholm, Sweden, 2025).
57. Weiß, M. et al. Multiharmonic frequency-chirped transducers for surface-acoustic-wave optomechanics. *Phys. Rev. Appl.* **9**, 014004 (American Physical Society, 2018).
58. Thevenard, L. et al. Surface-acoustic-wave-driven ferromagnetic resonance in (Ga, Mn) (As, P) epilayers. *Phys. Rev. B* **90**, 094401 (2014).
59. Rovillain, P. et al. Impact of spin-wave dispersion on surface-acoustic-wave velocity. *Phys. Rev. Appl.* **18**, 064043 (2022).
60. Vythelingum, A. K. et al. Role of coercivity in surface acoustic wave driven ferromagnetic resonance. *ACS Appl. Electron. Mater.* **7**, 4055–4064 (2025).
61. Xu, M. et al. Nonreciprocal surface acoustic wave propagation via magneto-rotation coupling. *Sci. Adv* **6**, eabb1724 (2020).
62. Robbins, W. P. A simple method of approximating surface acoustic wave power densities. In *IEEE Trans. Sonics Ultrason*. **24**, https://doi.org/10.1109/T-SU.1977.30956 (1977).
63. Rettner, C. T., Best, M. E. & Terris, B. D. Patterning of granular magnetic media with a focused ion beam to produce single-domain islands at > 140 Gbit/in2. *IEEE Trans. Magnet*. **37**, https://doi.org/10.1109/20.950927 (2001).
64. Krone, P. et al. Investigation of the magnetization reversal of a magnetic dot array of Co/Pt multilayers. *J. Nanoparticle Res.* **13**, 5587–5593 (2011).
65. Grobis, M. K., Hellwig, O., Hauet, T., Dobisz, E. & Albrecht, T. R. High-density bit patterned media: magnetic design and recording performance. *IEEE Trans. Magnet*. **47**, https://doi.org/10.1109/TMAG.2010.2076798 (2011).

Acknowledgements

This research was funded in whole or in part by the Austrian Science Fund (FWF) [DOI: 10.55776/I6068 & 10.55776/P34671] and by the Deutsche Forschungsgemeinschaft (DFG, German Research Foundation) project No. 504150161. We acknowledge the financial support of the Vienna Doctoral School in Physics (VDSP). For open access purposes, the author has applied a CC BY public copyright license to any author-accepted manuscript version arising from this submission.

Author contributions

D.S., H.J.K., M.A., and C.A. conceived the islet design. M.K.S. and C.A. formulated the unidirectional model. M.K.S. performed and analyzed all

micromagnetic simulations. E.D.S.N. and M.W. carried out all finite element simulations. P.F. implemented the magneto-elastic solver in magnum.np and analyzed the finite element simulations. M.K. performed the experiment used to validate the unidirectional model. M.K., S.G., H.J.K., and M.A. guided the device design using their experimental expertise. D.S., H.J.K., M.A., and C.A. jointly supervised the work. M.K.S. wrote the original draft with help from all other authors.

Competing interests

The authors declare no competing interests.

Additional information

Supplementary information The online version contains supplementary material available at https://doi.org/10.1038/s44306-026-00132-4.

Correspondence and requests for materials should be addressed to Michael K. Steinbauer.